JASA ARTICLE

# Experimental acoustic scene analysis using One-Eighth spherical fraction microphone array

T. Blanchard,[1,a)] P. Lecomte,[2] M. Melon,[1,b)] L. Simon,[1,c)] K. Hassan,[1] and R. Nicol[3]

[1]*Laboratoire d'Acoustique de l'Université du Mans (LAUM), UMR 6613, Institut d'Acoustique - Graduate School (IA-GS), CNRS, Le Mans Université, France*

[2]*University of Lyon, Université Claude Bernard Lyon 1, CNRS, Ecole Centrale Lyon, INSA Lyon, LMFA, UMR5509, 69622 Villeurbanne, France*

[3]*Orange Labs, 2 Avenue Pierre Marzin, 22307 Lannion Cedex, France*

**ABSTRACT:**

This paper investigates the performance of one-eighth Spherical Fraction Microphone Array through experimental measurement to analyze acoustic scenes in one-eighth of space. The array geometry is designed to be placed in a room corner at the junction of three acoustically rigid walls. Two prototypes are built with 8 and 16 microphones, respectively. The sampling strategy is discussed and a spatial aliasing analysis is carried out both analytically and by numerical simulations. The array performances are evaluated through Spherical Fraction Beamforming (SFB). This approach is based on the decomposition of the acoustic pressure field in a rigid bounded domain. The localization angular error and Directivity Index criterion are evaluated for both arrays. In a first experiment, the arrays are mounted in an eighth of space built inside an anechoic room. The results are compared with simulation and show consistency. The theoretical limitations of SFB in a rigid bounded one-eighth of space are retrieved experimentally. These limitations are also observed in a real configuration: an office room. Further investigations on SFB are also conducted in the case of a virtual scene constructed with two sound sources. © *2022 Acoustical Society of America.*

https://doi.org/10.1121/10.0009230

(Received 25 March 2021; revised 9 December 2021; accepted 9 December 2021; published online 10 January 2022)

[Editor: Mingsian R. Bai] Pages: 180–193

## I. INTRODUCTION

Microphone arrays are widely used in multiple scenarios such as sound field analysis,[1] sound enhancement,[2] or source localization.[3,4] In particular, Spherical Microphone Arrays (SMA)s have been widely studied for their ability to capture or to represent the acoustic pressure field with Spherical Harmonics (SHs). The analysis performance of the sound field captured by the SMA depends on the degree of the expansion over a SH basis[5,6] based on the Spherical Fourier Transform (SFT). The projection of the sound field on this basis is particularly of interest for beamforming applications due to its rotationnally invariant beamforming property.[7]

More recently, the use of Spherical Fraction Microphone Arrays (SFMAs) was shown to be relevant for sound field analysis when the acoustic sources are located within a limited angular sector. For example, Li and Duraiswami[8] proposed the use of an hemispherical-shape array of microphones to focus the sound capture on a half space bounded by a rigid plane for an usage in conference rooms. Their approach relies on the use of source and microphone images obtained from the rigid plane to form a virtual SMA. Another way to consider this task is to build a new basis of orthogonal functions onto the spherical sector domain where the sources are located. This new basis can be built either by orthogonalizing the actual SH basis yielding to spherical Slepian functions[9] or by scaling and shifting the associated Legendre polynomials and exponentials (respectively, cosine/sine) functions of complex (respectively, real) SHs.[10,11] Another approach is to take into account the spherical sector boundary conditions in the Helmholtz equations[12,13] to obtain a different orthogonal basis of harmonics for modal sound field decomposition within a limited range of directions.[14–16]

In Ref. 16, a theoretical study of Spherical Fraction Beamforming (SFB) has been conducted in the case of one-eighth, quarter, and half of spherical domain with acoustically-rigid boundary conditions. These domains can be easily approximated in common situations where a corresponding SFMA can be used. For instance, in a corner of a room for a one-eighth SFMA, at the junction of a wall and the ceiling for a quarter SFMA and either on a wall, ceiling, or floor for a half SFMA. The room walls and ceiling are therefore considered acoustically-rigid. The limitation of the $4\pi$-steradian solid angle to a smaller spherical sector of interest among 1/8, 1/4, or 1/2 sphere implies the extraction of a specific SH sub-basis from the SH basis to take into account the rigid boundary conditions. These functions are called Spherical Fraction Harmonics (SFHs).

In the present study, experimental characterizations of two rigid one-eighth SFMAs for SFB are carried out. A preliminary study has been presented in Ref. 17. Here, two

a)Electronic mail: torea.blanchard@hotmail.fr
b)ORCID: 0000-0002-7167-9909.
c)ORCID: 0000-0001-6115-9160.

 

https://doi.org/10.1121/10.0009230

one-eighth SFMAs with different radii and number of microphones are studied. First, a study of spatial aliasing is proposed, through numerical simulations and analytical analysis. Then, the beamforming performance of SFMAs is evaluated with Direction of Arrival (DOA) angular error and Directivity Index (DI). Measurements are performed both in one-eighth of an anechoic room and in a conventional office room for which the SFMAs are mounted at a room corner. The Impulse Responses (IR)s are measured for each microphone of the SFMAs and for different source locations, and are used to create virtual acoustic scenes where spatial filtering is applied. The ability of the beamformer to extract the acoustic signal coming from each source is evaluated by estimating the correlation amount between each spatially filtered signal and the original ones.

This paper is organized as follows: In Sec. II the SFB theory is recalled for one-eighth of a sphere domain with rigid boundary condition. The corresponding SFHs are presented as well as the performances criteria employed to characterize the SFMAs. In Sec. III, the SFMAs design and building are presented. In particular, the spatial aliasing errors are considered. The SFB results, both for DOAs estimation and signal audio extraction are presented and discussed in Sec. IV. Finally, the paper is concluded in Sec. V.

## II. THEORETICAL BACKGROUND

### A. SFH

This section briefly outlines the main results from Ref. 16 that are called to conceive the proposed application. In this work, one-eighth of the unit sphere $\mathbb{S}$ is considered as shown in Fig. 1. This domain is defined by its azimuth and elevation angle ranges, $\phi$ and $\theta$ respectively, as

$$\mathbb{F}_{1/8} = \left\{(\theta,\phi) \in \mathbb{S} \,|\, 0 \le \theta \le \frac{\pi}{2}, 0 \le \phi \le \frac{\pi}{2}\right\}. \tag{1}$$

The one-eight of Euclidian space of radius $r$ is noted $\mathbb{O}_{1/8}$, with

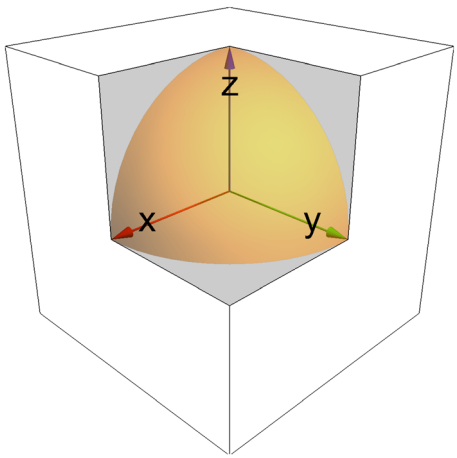


FIG. 1. (Color online) One-eighth of the unit sphere $\mathbb{F}_{1/8}$, with acoustically-rigid boundary conditions on the planes $x = 0$, $y = 0$, and $z = 0$ (in gray).

$$\mathbb{O}_{1/8} = \{(\theta,\phi,r) \in \mathbb{F}_{1/8} \times \mathbb{R}^+\}. \tag{2}$$

Acoustically-rigid boundary condition is imposed on the planes $x = 0$, $y = 0$, and $z = 0$ as shown in gray in Fig. 1. In Ref. 16, it was shown that the angular part of the solution of the homogeneous spherical Helmholtz equation in $\mathbb{O}_{1/8}$ are the SFHs noted $Y_{l,m,1/8}(\theta,\phi)$ and defined by

$$Y_{l,m,1/8}(\theta,\phi) = 2\sqrt{2}Y_{l,m}(\theta,\phi) \text{ for } (l,m) \in \mathbb{M}_{1/8}. \tag{3}$$

In Eq. (3), $\phi \in ]0, 2\pi]$ and $\theta \in [0,\pi]$, $l$ is the degree, $m$ is the order with $|m| \le l$. The real SHs, $Y_{l,m}(\theta,\phi)$, are given by

$$Y_{lm}(\theta,\phi) = N_{l,|m|}P_l^m(\cos\theta) \times \begin{cases} \cos(|m|\phi) & \text{for } m \ge 0 \\ \sin(|m|\phi) & \text{for } m < 0 \end{cases}, \tag{4}$$

where $P_l^m$ are the associated Legendre polynomial of the first kind of degree $l$ and order m, with $|m| \le l$, and $N_{l,|m|}$ is a normalization factor given by

$$N_{l,|m|} = \sqrt{\frac{(2-\delta_m)(2l+1)}{4\pi}\frac{(l-|m|)!}{(l+|m|)!}}, \tag{5}$$

where $\delta_m$ stands for the Kronecker delta function and ! indicates the factorial operator. The set $\mathbb{M}_{1/8}$ is defined by

$$\mathbb{M}_{1/8} = \{(l,m) \in \mathbb{N} \times \mathbb{Z} \,|\, l \bmod 2 = 0 \wedge m \bmod 2 = 0 \wedge m \ge 0\}, \tag{6}$$

where $[.]$ and $\wedge$ are the modulo and logical and operators, respectively. The basis of SFHs $Y_{l,m,1/8}$ is derived from the SH basis by selecting the functions which present even symmetry with respect to the planes $x = 0, y = 0$, and $z = 0$ simultaneously. The set of indices $\mathbb{M}_{1/8}$ allows to select these SHs: their degree $l$ is even and their order $m$ is positive and even. The factor $2\sqrt{2}$ in Eq. (3) ensures the orthonormality property of the SFH basis on $L^2(\mathbb{F}_{1/8})$, the space of square-integrable function in $\mathbb{F}_{1/8}$.

Up to a degree $L$, the number of SFHs $Y_{l,m,1/8}$ is denoted $Q(L)$ with

$$Q(L) = \frac{1}{2}\left(\left\lfloor\frac{L}{2}\right\rfloor + 1\right)\left(\left\lfloor\frac{L}{2}\right\rfloor + 2\right), \tag{7}$$

where $\lfloor\cdot\rfloor$ is the floor operator. The number $Q(L)$ represents the minimum number of microphones for an accurate decomposition, i.e., $N_{1/8} \ge Q(L)$,[14] where $N_{1/8}$ is the number of microphones that constitute the one-eighth SFMA. This number converges to 8 times less the number of SH, $(L+1)^2$, as $L$ increases.[16]

### B. Representation of acoustic pressure field with SFHs

The acoustic pressure in the domain $\mathbb{O}_{1/8}$ can be expressed with SFHs $Y_{l,m,1/8}$ as

$$p(k,r,\theta,\phi) = \sum_{\substack{l=0 \\ (l,m)\in\mathbb{M}_{1/8}}}^{\infty} \sum_{m=-l}^{l} p_{l,m,1/8}(kr) Y_{l,m,1/8}(\theta,\phi). \quad (8)$$

In Eq. (8), $p_{l,m,1/8}$ are the acoustic pressure field coefficients obtained with the SPHT,[16]

$$p_{l,m,1/8} = \int_{\mathbb{F}_{1/8}} p(k,r,\theta,\phi) Y_{l,m,1/8}(\theta,\phi) \sin(\theta) \mathrm{d}\theta \mathrm{d}\phi. \quad (9)$$

### C. Estimation of acoustic pressure coefficients

In this paper, the acoustic pressure is measured on the surface of a rigid one-eighth of a sphere of radius $r_a$. In this case one has[5]

$$p_{l,m,1/8} = \frac{i^{l-1}}{(kr_a)^2 h_l'(kr_a)} b_{l,m,1/8}, \quad (10)$$

where $i$ is the imaginary unit and $h_l'$ are the first derivative, with respect to its argument, of the spherical Hankel functions of second kind and degree $l$. The terms $b_{l,m,1/8}$ are the radius-independent acoustic pressure field coefficients. For a plane wave with DOA $(\theta_s, \phi_s)$, they are expressed as[16]

$$b_{l,m,1/8} = Y_{l,m,1/8}(\theta_s, \phi_s). \quad (11)$$

The estimation of the acoustic pressure coefficients $b_{l,m,1/8}$ can be retrieved from the $p_{l,m,1/8}$ coefficients with Eq. (10). In practice, this is unfeasible at low $kr_a$ where excessive amplification due to Hankel functions occurs. Therefore, a Thikhonov regularization is used and the estimated coefficients $\tilde{b}_{l,m,1/8}$ are given by[5]

$$\tilde{b}_{l,m,1/8} = \frac{1/E_l(kr_a)^*}{|1/E_l(kr_a)|^2 + \lambda^2} p_{l,m,1/8}, \quad (12)$$

where $E_l(kr_a) = i^{1-l}(kr_a)^2 h_l'(kr_a)$ are the inverse of radial function in Eq. (10), $^*$ is the conjugate, and $\lambda$ is a regularization parameter.

### D. SFB

The acoustic pressure energy in $\mathbb{F}_{1/8}$ can be visualized using the Steered Response Power (SRP) of a SFB. The SFB output signal $y(k,\theta,\phi)$ is computed up to degree $L$ with

$$y(k,\theta,\phi) = \sum_{\substack{l=0 \\ (l,m)\in\mathbb{M}_{1/8}}}^{L} \sum_{m=-l}^{l} w_{l,m} b_{l,m,1/8}, \quad (13)$$

where $w_{l,m}$ are the beampattern weights. For a regular beampattern with steering angle $(\theta,\phi)$ one has[16]

$$w_{l,m} = Y_{l,m,1/8}(\theta,\phi). \quad (14)$$

The beamformer SRP is given by the square magnitude of $y(k,\theta,\phi)$ for all possible $(\theta,\phi)$.

### E. Array performances

#### 1. Source localization

The DOA of a sound source is estimated through SRP maximization of the beamformer output as given in Eq. (13) on a given discrete grid. The error with respect to the true direction is given by the angle difference $\Theta$ between the estimated DOA and the true one. This angle is given by

$$\cos(\Theta) = \sin(\hat{\theta})\sin(\theta_s)\cos(\hat{\phi} - \phi_s) + \cos(\hat{\theta})\cos(\theta_s), \quad (15)$$

where $(\hat{\theta}, \hat{\phi})$ is the estimated DOA.

#### 2. DI

The performance of the array is also evaluated using the Directivity Factor (DF) adapted for the case of a one-eighth of sphere

$$\mathrm{DF}(k,\hat{\theta},\hat{\phi}) = \frac{|y(k,\hat{\theta},\hat{\phi})|^2}{\frac{2}{\pi}\int_{\mathbb{F}_{1/8}} |y(k,\theta,\phi)|^2 \sin(\theta) d\theta d\phi}. \quad (16)$$

Note that the integral in Eq. (16) is restricted to $\mathbb{F}_{1/8}$, i.e., the angular sector viewed by the one-eighth of sphere. The DI is then computed from Eq. (16) into decibel scale with

$$\mathrm{DI}(k,\hat{\theta},\hat{\phi}) = 10\log_{10}(\mathrm{DF}(k,\hat{\theta},\hat{\phi})). \quad (17)$$

## III. DESIGN AND REALIZATION OF ONE-EIGHTH SPHERICAL FRACTION MICROPHONE ARRAYS

In this section, the choice of microphone numbers and positions, the spatial aliasing study, and some building details for two one-eighth SFMAs are reported.

### A. Microphone positions

In order to estimate the coefficients $p_{l,m,1/8}$ in Eq. (10) from discrete measurements with microphones, a quadrature rule working on $\mathbb{F}_{1/8}$ is used for the microphone positions. To find such quadrature, one starts with a Gauss-Legendre quadrature rule on the whole sphere[6] and the symmetries of the problem are used.

#### 1. Gauss-Legendre quadrature

The Gauss-Legendre quadrature on the whole sphere samples equally along the azimuth angle and the zenith angles correspond to the roots of the Legendre polynomial $P_{L+1}(\cos\theta)$ where $L$ is the maximum degree of decomposition. The total number of nodes for this mesh is $N = 2(L+1)^2$. The node positions and weights are given by the following formulas:[18]

https://doi.org/10.1121/10.0009230

$$\begin{cases} \phi_n = \left(n+\frac{1}{2}\right)\frac{2\pi}{2L+2}, \quad n \in \{0,\ldots,2L+1\} \\ P_{L+1}(\cos(\theta_q)) = 0, \quad q \in \{0,\ldots,L\} \\ \alpha_q = \frac{\pi}{L+1}\frac{2(1-\cos(\theta_q)^2)}{(L+2)^2(P_{L+2}(\cos(\theta_q))^2}, \quad q \in \{0,\ldots,L\}. \end{cases} \tag{18}$$

#### 2. Mesh symmetry for odd degree L

From Eq. (18), for an odd degree $L$, there are $L+1$ even number of roots for $P_{L+1}(\cos(\theta)) = 0$. The corresponding directions $\theta_q$, are grouped by pairs, which are symmetric to the plane $z = 0$ without possibility of north and south pole directions. In addition, there are an even number of azimuth directions $\phi_n$, which are symmetrical with respect to the $x = 0$ and $y = 0$ planes. Note that the starting angle for $n = 0$ in Eq. (18) ensures that no nodes will be on the planes $x = 0$ or $y = 0$. This choice is made to facilitate the mounting of microphone during the prototype building. Finally, the resulting mesh presents symmetries with respect to the planes $x = 0$, $y = 0$, and $z = 0$. Then, by retaining only the nodes belonging to one-eighth of a sphere, the total number of nodes is reduced to $N_{1/8} = N/8$, where the quadrature rule of Eq. (18) is suitable in the domain $\mathbb{F}_{1/8}$ to estimate the coefficients $p_{l,m,1/8}$ as

$$p_{l,m,1/8} = \sum_{n=0}^{(L-1)/2}\sum_{q=0}^{(L-1)/2} \alpha_q p(k,r,\theta_q,\phi_n) Y_{l,m,1/8}(\theta_q,\phi_n). \tag{19}$$

The demonstration of Eq. (19) is done with the image source principle and provided in Appendix A. The summations up to $(L-1)/2$ are explained using the symmetrical properties of the SFHs.

### B. Prototype building

Two one-eighth SFMA prototypes are built. They are shown in Fig. 2. The first prototype possesses eight microphones [Fig. 2(a)], while the second prototype inludes 16 microphones [Fig. 2(b)]. To allow the instrumentation assembly inside the prototypes, a spherical shell geometry is chosen. It is realized by Fused Deposition Modeling three-dimensional (3D)-printing in PolyLactic Acid plastic. The shell thickness is 15 mm with an external radius $r_a$. The microphones are omnidirectional digital Micro-Electro-Mechanical System (MEMS) microphones Knowles® SPH0645LM4H for the 8-microphone array and InvenSense® ICS-52000 for the 16-microphone array. The MEMS microphones are presoldered on Printed Circuit Boards (PCB) and clipped on the shell. The wiring to a MiniDSP™ USBStreamer sound card place inside the shell is ensured using Dupont® prototype cables connected to a custom-made PCB.

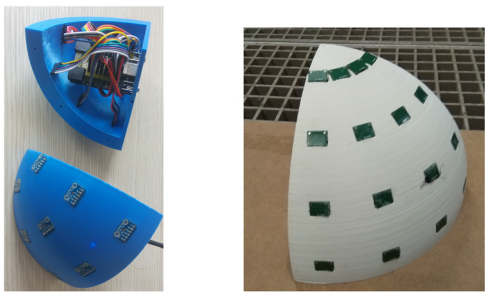

(a) (b)

FIG. 2. (Color online) (a) 8 MEMS microphone one-eighth SFMA with external radius $r_a = 10$ cm. (b) 16 MEMS microphone one-eighth SFMA with external radius $r_a = 17$ cm.

In the following paragraphs, specific details are given on each SFMA.

#### 1. 8-microphone SFMA

For this array, a Gauss-Legendre quadrature on the whole sphere is chosen with $L=5$.[17] In this case, the number of microphones on the one-eighth of sphere should be $N_{1/8} = 9$. However, the size of the MEMS microphone PCBs used for the prototype building limits their assembly on the prototype shell. Moreover, the soundcard available for connecting the microphones allows only eight channels when using I2S (Integrated Interchip Sound) protocol. Therefore, it was chosen to remove a node [in red on Fig. 3(a)] and the number of microphones is reduced to $N_{1/8} = 8$. Thus, the quadrature rule given in Eq. (19) is no longer suitable. Estimation of coefficients $p_{l,m,1/8}$ in Eq. (8) is therefore achieved by an inverse problem approach[5] as a solution in a least-square sense given by

$$\mathbf{p}_{L,1/8} = \mathbf{Y}_L^{\dagger}\mathbf{p}, \tag{20}$$

where $\mathbf{p}_{L,1/8} \in \mathbb{C}^{Q(L)\times 1}$ is the vector of SFH coefficients up to degree $L$, $\mathbf{p} \in \mathbb{C}^{N_{1/8}\times 1}$ is the vector of acoustic pressure at the microphones, $\mathbf{Y}_L \in \mathbb{R}^{N_{1/8}\times Q(L)}$ is a matrix containing the SFHs evaluated at the nodes directions up to degree $L$, $\mathbf{Y}_L^{\dagger} = (\mathbf{Y}_L^T\mathbf{Y}_L)^{-1}\mathbf{Y}_L^T \in \mathbb{R}^{Q(L)\times N_{1/8}}$ is the Moore-Penrose pseudo-inverse of $\mathbf{Y}_L$. Note that this approach can be used as long as the number of nodes is superior or equal to $Q(L)$.[5] The radius of this prototype is $r_a = 10$ cm.

#### 2. 16-microphone SFMA

The second prototype is designed from a Gauss-Legendre quadrature rule working up to degree $L = 7$. Here, $N_{1/8} = 16$ microphones are mounted on the shell of the one-eighth of sphere. The mesh for this prototype is shown in Fig. 3(b) and Eq. (19) is used to compute the SFH coefficients. For this prototype, the Time-Division Multiplexing (TDM) protocol is used in order to allow the synchronization of 16 TDM MEMS microphones. The radius of this array is $r_a = 17$ cm.

### C. Spatial aliasing study

#### 1. Orthonormality error

As the acoustic pressure field coefficients $p_{l,m,1/8}$ in Eq. (8) are not null for degree $l > L$, spatial aliasing occurs when using Eq. (19) or Eq. (20). Spatial aliasing errors are driven by the orthonormality errors when integrating a product of

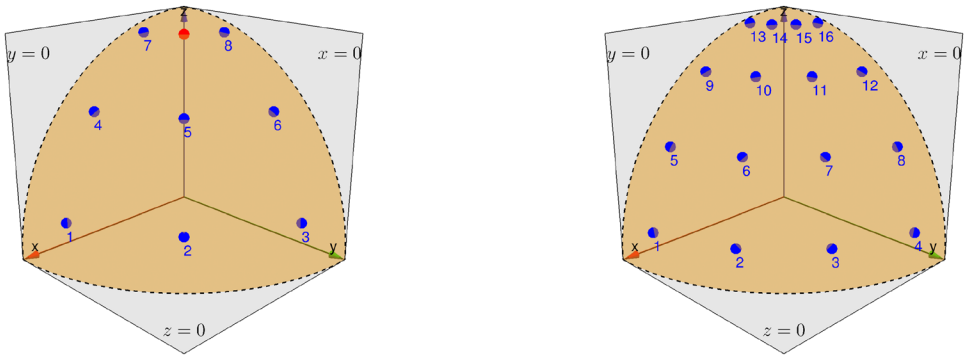


(a) (b)

FIG. 3. (Color online) Sampling schemes of the two one-eighths of sphere where blue nodes are the real microphone positions. (a) Mesh of the first one-eighth SFMA with $N_{1/8} = 8$ where the red node has been removed. (b) Mesh of the second one-eighth SFMA with $N_{1/8} = 16$.

two SFHs using Eqs. (19) or (20).[19] The orthonormality error matrix $\mathbf{D}$ allows to quantify such errors. It is defined by

$$\mathbf{D} = \begin{cases} \mathbf{Y}_L^T \mathbf{W} \mathbf{Y}_{L'} - \mathbf{I} & \text{when using Eq. (19)} \\ \mathbf{Y}_L^\dagger \mathbf{Y}_{L'} - \mathbf{I} & \text{when using Eq. (20)} \end{cases}, \quad (21)$$

where $\mathbf{I} \in \mathbb{R}^{Q(L)\times Q(L')}$ has 1 on its diagonal and 0 elsewhere, $\mathbf{W} \in \mathbb{R}^{N_{1/8}\times N_{1/8}}$ is the matrix of quadrature weights given in Eq. (18) and $\mathbf{Y}_{L'}$ is the SFH matrix of dimension $N_{1/8} \times Q(L')$ with $L' \geq L$.

The corresponding numerically-calculated orthonormality error matrices are plotted in Fig. 4(a) for the 8-microphone array and in Fig. 4(b) for the 16-microphone array. The matrices are computed with $L = 4$ for the 8-microphone SFMA and $L = 6$ for the 16-microphone SFMA. For both arrays, the orthonormality errors are shown up to degree $L' = 12$. The value $\mathbf{D}_{ij}$ located at the $i$th row and $j$th column indicates the aliasing error value between the $i$th SFH and the $j$th SFH, where the indices $i$ and $j$ increase as $l^2 + l + m$ and $l'^2 + l' + m'$, respectively. The indices $(l, m)$ and $(l', m')$ in $\mathbb{M}_{1/8}$. The higher the value is, the greater the aliasing is. It can be observed that the orthogonormality errors are negligible up to degree $L = 4$ for the 8-microphone array and up to $L = 6$ for the 16-microphone array. For higher degrees, high errors emerge.

### 2. Aliasing function study

The aliasing function obtained when using the Gauss-Legendre quadrature of Eq. (18) on a one-eighth of sphere is investigated. In fact, using Eq. (19) with a function $Y_{l'm',1/8}$ instead of $p(k, r, \theta_q, \phi_n)$ leads to

$$\sum_{n=0}^{(L-1)/2} \sum_{q=0}^{(L-1)/2} \alpha_q Y_{l,m,1/8}(\theta_q, \phi_n) Y_{l',m',1/8}(\theta_q, \phi_n) = \delta_{l-l'}\delta_{m-m'} + \epsilon(l, l', m, m'), \quad (22)$$

$\epsilon$ represents the aliasing function. Following the study in Ref. 20, explicit formulas are given on the indices $(l, l', m, m')$ for $\epsilon(l, l', m, m')$ to be null. Note that in the present study, real SFHs are used on a one-eighth of a spherical mesh instead of complex SHs on the whole spherical mesh as done in Ref. 20, which brings different results. It is shown that for $l \leq L$,

$$\epsilon(l, l', m, m') = \begin{cases} 0 \text{ for } l + l' \leq 2L + 1 \\ 0 \text{ for } (m + m') \bmod (4L + 4) = 0 \wedge (m - m' + 2L + 2) \bmod (4L + 4) = 0 \\ 0 \text{ for } (m + m' + 2L + 2) \bmod (4L + 4) = 0 \wedge (m - m') \bmod (4L + 4) = 0 \\ 0 \text{ for } (m + m') \bmod (2L + 2) \neq 0 \wedge (m - m') \bmod (2L + 2) \neq 0. \end{cases} \quad (23)$$

These relationships help to predict the orthonormality error, as in Fig. 4(b).

## IV. ARRAY CHARACTERIZATION

### A. Measurement set-up

In order to assess the array performances both in the anechoic condition and a more realistic scenario of a conventional office room, a loudspeaker is used as an acoustic source at a known DOA. A 2-in. and a 3-in. AuraSound® loudspeakers are used in the anechoic room and the conventional office room, respectively. The IRs between the driving voltage signal of the loudspeaker and the microphone signals are measured with exponential swept sine method. The starting and ending frequency are $f_{\text{start}} = 200$ Hz and $f_{\text{end}} = 8$ kHz, respectively. The excitation

https://doi.org/10.1121/10.0009230

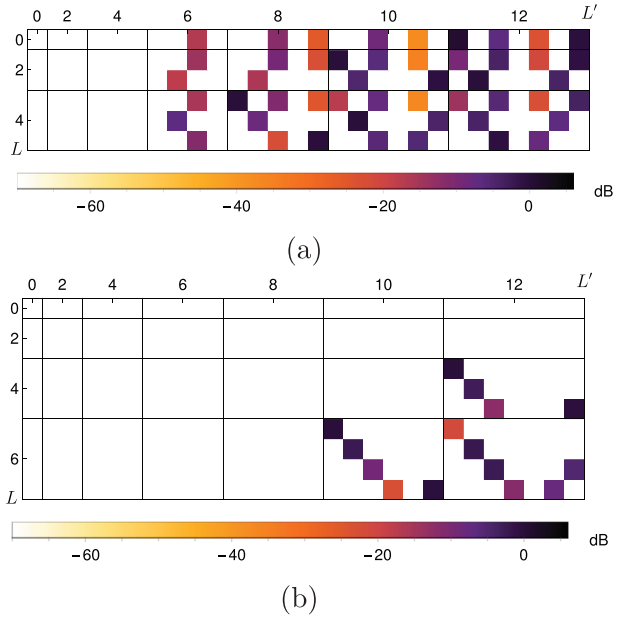


FIG. 4. (Color online) Orthonormality error matrices $\mathbf{D}$ up to degree $L' = 12$ for the two prototypes composed of (a) 8 microphones with $L = 4$, (b) 16 microphones with $L = 6$.

signal duration is 8 s with a sampling frequency of 44.1 kHz. Based on the IRs, the coefficients $p_{l,m,1/8}$ are estimated with Eq. (20) for the 8-microphone array and with Eq. (19) for the 16-microphone one. Then, the coefficients $\tilde{b}_{l,m,1/8}$ are estimated with Eq. (12), where the regularization parameter $\lambda$ is chosen to a corresponding signal to noise ratio of $g_s = 50$ dB.[5] The SRP is computed with the regular beampattern weights given in Eq. (14). The SRP maps are computed with angular resolutions of $\Delta\theta = \Delta\phi = 0.9°$.

## B. Anechoic room

### 1. Measurement conditions

For this experiment, a one-eighth of anechoic space is constructed using three $2 \times 2\,\mathrm{m}^2$ wooden panels assembled in a corner at which the SFMA under test is mounted. This set-up can be shown in Fig. 5. The loudspeaker is fixed at $R_{\mathrm{LS}} = 1$ m radial distance from the corner, on a metal hoop, such that it can be moved over each node of a one-eighth spherical grid as shown in Fig. 6. The mesh is sampled into $17 \times 17$ nodes at angles ranging from 5° to 85° equi-spaced in azimuth and zenith with 5° steps.

### 2. Beamforming result

The experimental normalized SRP maps, calculated for $kr_a = 4.5$ both for the 8-microphone array (2nd column) and for the 16-microphone one (4th column), are shown in Fig. 7 for three positions of the loudspeaker. The first position (1st row) is (45°, 45°), the second one (2nd row) is (30°, 20°) and the third one (3rd row) is (60°, 60°). The two last positions are chosen to be close to the wall while the first one is taken in the center of the spherical grid. Note that the boundaries that form the corner are located at $\phi = 0°$, $\phi = 90°$, and $\theta = 90°$, respectively. Note also that the position (20°, 30°) is closer to the boundary than the position (60°, 60°). The theoretical SRP maps given both for the 8-microphone array (1st column) and the 16-microphone one (3rd column) are computed for a plane wave source [Eq. (11)].

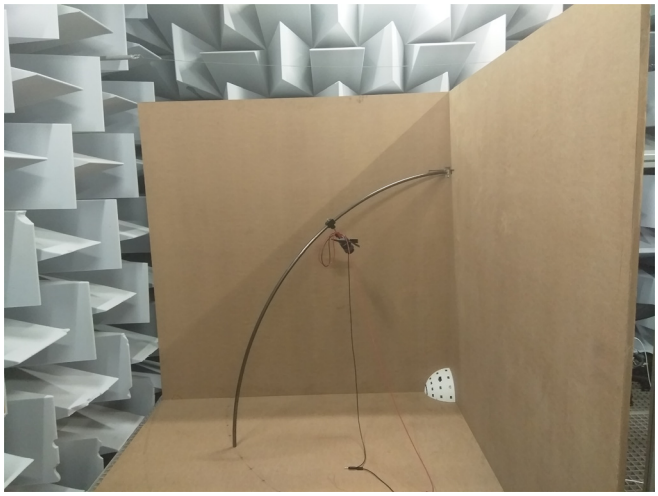

FIG. 5. (Color online) Experimental set-up mounted in the anechoic room where a one-eighth SFMA (here the 16-microphone array) can be placed at the corner formed by three $2 \times 2\,\mathrm{m}^2$ wooden panels. A loudspeaker is fixed on a metal hoop at $R_{\mathrm{LS}} = 1$ m from the corner.

The SRP maps obtained from the experimental measurements are similar to those simulated when compared to the aforementioned performance criteria. In all instances, the mainlobe is larger with the 8-microphone array with a smaller DI. The larger mainlobe obtained with the 8-microphone array is explained by a smaller maximum degree of decomposition. The estimation of the source position is accurate for both arrays when the source is located in the center of the grid [position (45°, 45°)]. However, accuracy can deteriorate when the source is close to the one-eighth space boundary. This can be explained by the fact that the beampattern shape is changed due to the presence of the rigid boundaries. According to the image source principle, the beampattern obtained in $\mathbb{F}_{1/8}$ is the same as adding

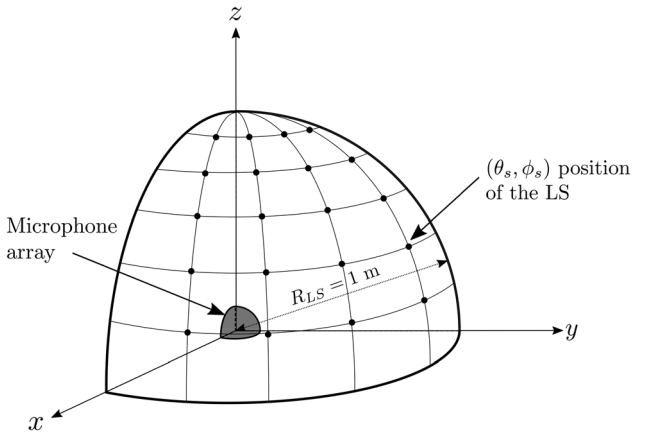


FIG. 6. Mesh for the measurement of impulse responses from a loudspeaker (LS) positioned at each node of the mesh.

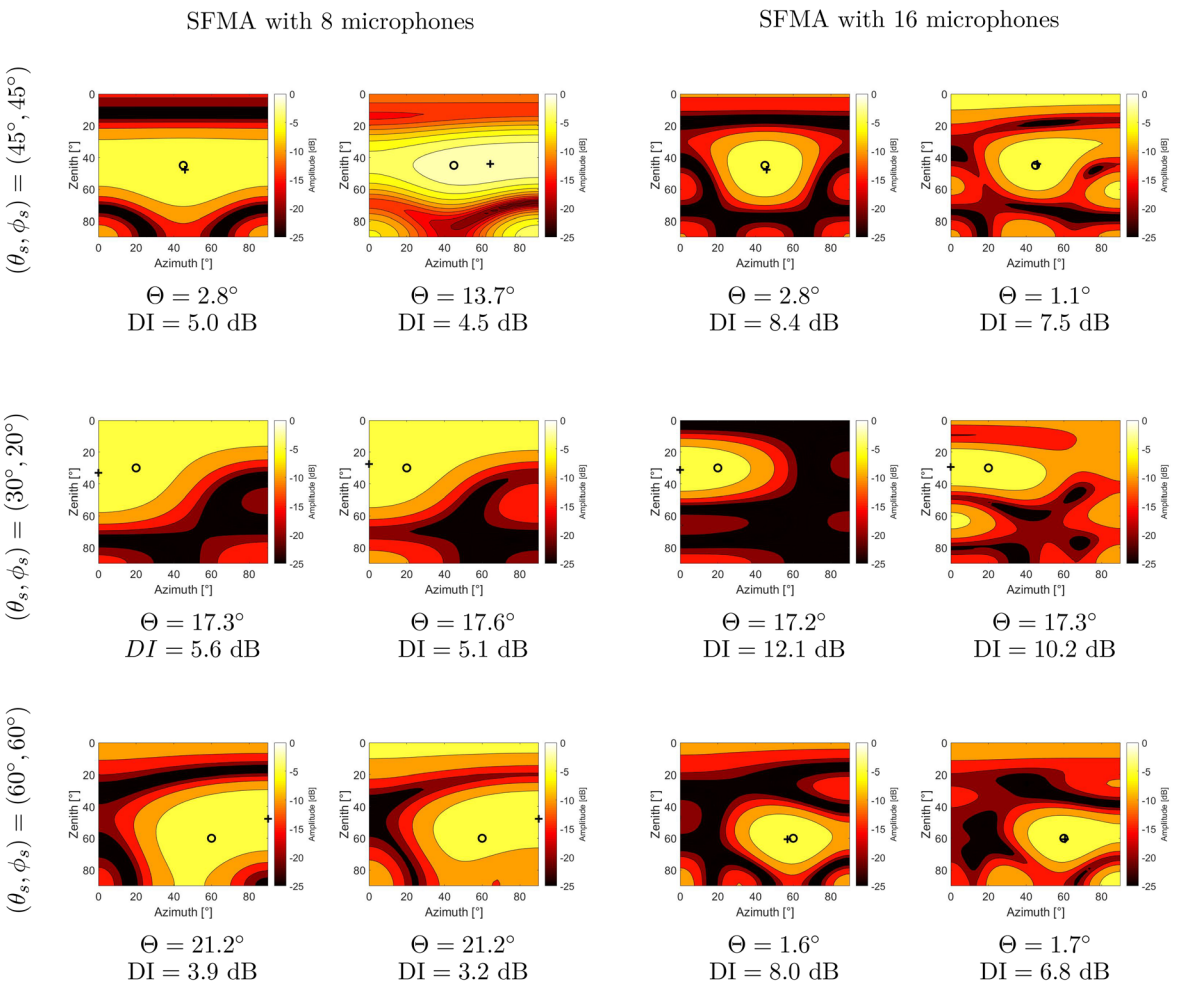


FIG. 7. (Color online) Comparison of the beamforming results with regular beampattern for three source DOAs both from simulation (1st and 3rd columns) and experimental measurements (2nd and 4th columns) conducted in anechoic room. The normalized squared beamfomer output $|y(k,\theta,\phi)|^2/|y(k,\theta_s,\phi_s)|^2$ is plotted over the steering directions $(\theta,\phi) \in [0°, 90°] \times [0°, 90°]$ for $kr_a = 4.5$. The cross-and circle symbols represent the estimated and the theoretical source positions, respectively.

the beampatterns calculated with a rigid full-sphere microphone array in the absence of reflecting walls with additional sources. The DOAs of the additional sources are symmetrical to the actual source DOA with respect to the planes forming the one-eighth of space. As a consequence, the closer the source DOA is to the boundary, the more the beampattern shape in $\mathbb{F}_{1/8}$ is modified. The modification of the beampattern shape is such that for a source with DOA closer to the boundary than a specific angle $\Theta_{\text{lim}}$, the maximum of the SRP is located at the boundary. This angle is defined as the full-width at maximum half (FWMH) of the mainlobe of the beampattern calculated with a rigid full-sphere microphone array in the absence of reflecting walls.[16]

From the reading of Fig. 6 in Ref. 16, the angle $\Theta_{\text{lim}}$ is approximately equal to 50° for $L = 4$ (which is the maximum degree of decomposition to avoid orhonormality errors in the case of the 8-microphone array). However, the source positions are at 20° and 30° to the closest boundary in position (20°, 30°) and (60°, 60°), respectively. Therefore, the mainlobe and its image overlap to form a lobe of greater amplitude where the maximum is located at the boundary. In the case of the 16-microphone array, $\Theta_{\text{lim}} \simeq 35°$. The superposition effect is significantly reduced for the position (60°, 60°) but remains dominant for the position (20°, 30°).

For further investigation, the DIs for the three positions of the loudspeaker are plotted as a function of the dimensionless spatial frequency $kr_a$ in Fig. 8. The results show a working frequency range with almost constant DI values between 6.5 and 10.6 dB from approximately $kr_a = 4.5$ to $kr_a = 16.1$ for the 16-microphone array, or equivalently from $f \simeq 1466$ to $f \simeq 5214$ Hz, i.e., a frequency bandwidth of $\Delta f = 3748$ Hz. In contrast, the working frequency range of the 8-microphone array starts from approximately $kr_a = 3.2$ to $kr_a = 11.4$, or equivalently from $f \simeq 1753$ to $f \simeq 6261$ Hz, i.e., a frequency bandwidth of $\Delta f = 4508$ Hz, with almost constant DI values between 2.9 and 5.9 dB. For high frequencies, spatial aliasing strongly degrades the performance for both arrays which results in a drop in DI values. The 16-microphone array performs better within the working frequency range with higher DI values than the ones calculated with the 8-microphone array. It is also worth noting that for both arrays higher DI values are calculated

https://doi.org/10.1121/10.0009230

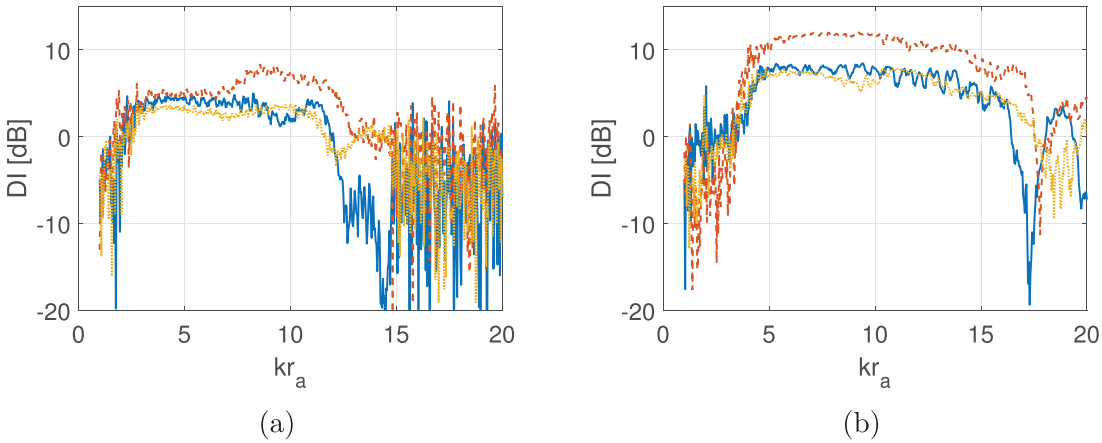


FIG. 8. (Color online) DI as a function of the dimensionless spatial frequency $kr_a$ from 1 to 20 for the 8-microphone array (a) and the 16-microphone array (b) for three source DOAs: $(45°, 45°)$ (blue solid line), $(30°, 20°)$ (red dashed line), and $(60°, 60°)$ (yellow dotted line).

for the source with DOA of $(30°, 20°)$. This is explained by the superposition of the lobe images with the mainlobe leading to a higher lobe amplitude. The effect of this phenomenon is less signifcant for the other source directions.

### 3. Frequency response function (FRF) study

In addition to the beamforming results given in Sec. IV B 2, a FRF analysis is performed. The FRF $|y(k, \theta, \phi)|$ is displayed along the zenith parameter, with a fixed azimuth angle $\phi = \phi_s$, as a function of the dimensionless spatial frequency $kr_a$. The FRFs for the arrays and for the three DOAs, as already proposed before, are given in Fig. 9. The zenith angle $\theta = \theta_s$ is highlighted with a solid line. The beam patterns show the presence of a well-defined mainlobe, in a specific range, approximately centered around the angle $\theta = \theta_s$, except in the case of the source with a DOA of $(30°, 20°)$, for which the shape of the mainlobe is more extensive. In accordance with the DI results, the 8-microphone array has a well-defined mainlobe over a range of about $kr_a = 3$ to $kr_a = 11$ against $kr_a = 4$ to $kr_a = 16$ in the case of the 16-microphone array. The performance of the arrays is clearly limited at high frequencies where several lobes, related to spatial aliasing, emerge.

## C. Two source scenario

A virtual acoustic scene is built using the IRs measured in the anechoic room. The IRs estimated from the positions (30°, 20°) (source $S_1$) and (60°, 60°) (source $S_2$) are convoluted to two linear chirp signals with same amplitude.

### 1. 8-microphone array result

The SRP calculation result with the 8-microphone array is given in Fig. 10(a) for $kr_a = 6$. Two regions with high and

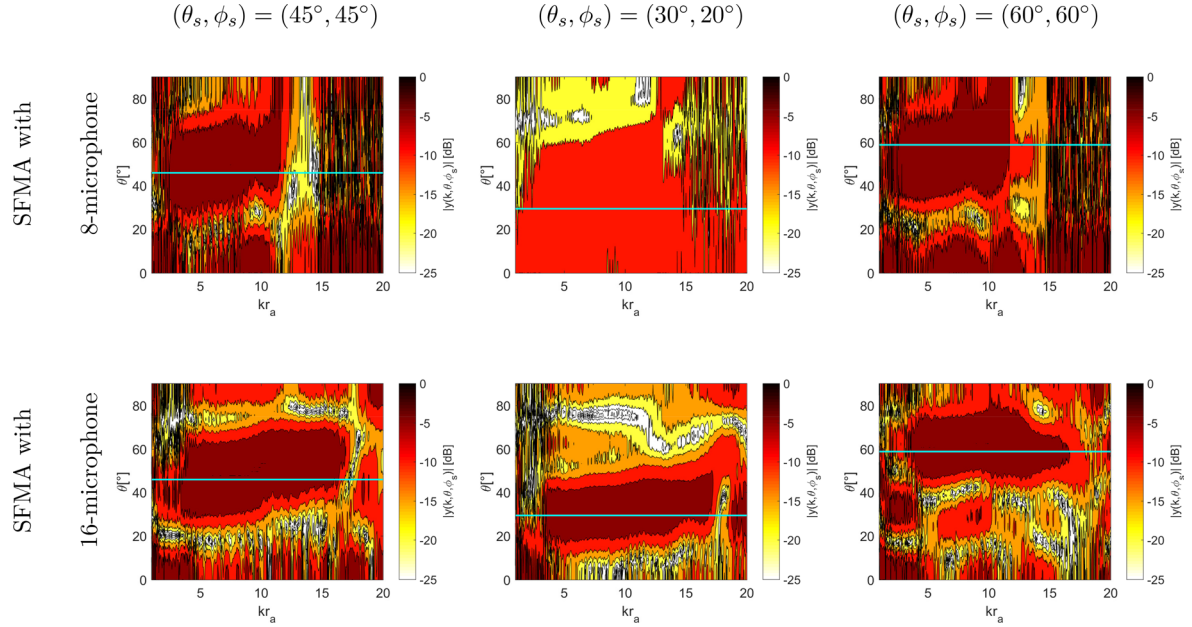


FIG. 9. (Color online) Frequency response function $|y(k, \theta, \phi)|$ at fixed azimuth $\phi = \phi_s$ of the 8-microphone and 16-microphone arrays as a function of the dimensionless spatial frequency $kr_a$ for three source DOAs. The solid line (cyan) gives the angle $\theta = \theta_s$.

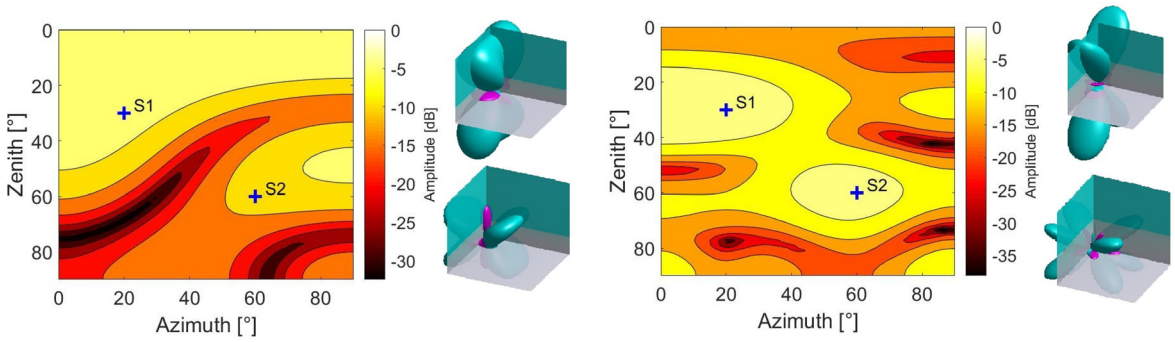


FIG. 10. (Color online) Normalized directivity map for a regular beampattern obtained both from the 8-microphone (a) and the 16-microphone (b) spherical fraction arrays for *kra=6* with two source DOAs $(30°, 20°)$ (source $S_1$) and $(60°, 60°)$ (source $S_2$) using the IRs calculated in the anechoic room. The true source positions are indicated by a blue cross. The $4\pi$-steradian associated beampatterns are given on the right in the direction of $S_1$ (up) and in the direction of $S_2$ (down). The gray planes depict the corner where the one-eighth of sphere is placed.

moderate energies around the direction of the sources (pointed out by a blue cross) $S_1$ and $S_2$, respectively, are visible. One could expect two main lobes with the same amplitude. However, the mainlobe in the direction of $S_1$ is most influenced by its closest symmetrical images. To better understand it, the $4\pi$-steradian directivity beampatterns calculated for a plane wave [Eq. (11)] are plotted at the right of the map for each direction where the one-eighth of space $\mathbb{O}_{1/8}$ is delimited by the corner formed by the gray planes. The beampattern for the direction of $S_1$ is given on the top while that of the direction of $S_2$ is shown below. The plots show a larger lobe in the first case. This is the result of the superposition of the three image lobes, located on the upper part, with the current lobe in $\mathbb{O}_{1/8}$, while only one image lobe influences significantly the mainlobe in $\mathbb{O}_{1/8}$ in the second case.

#### 2. 16-microphone array result

The SRP map as well as the directivity beampatterns obtained with the 16-microphone array are given in Fig. 10(b). As expected, the two lobes are narrower than the ones of the 8-microphone array. As for the results with the 8-microphone array, there is a difference in amplitude between the two lobes that can be explained by following the same approach. The beampattern shape when the array steers in the direction of $S_1$ shows four main lobes. They are the result of a superposition of lobes two-by-two, while, when the array steers in the direction of $S_2$, four lobes are clearly visible. In the latter case, the superposition effect is less pronounced because the source is located far enough from the boundary of the domain relatively to the FWMH of its mainlobe.

### D. Conventional office room

#### 1. Measurement conditions

For complementary experiments, the SFMAs are tested in a conventional office room as shown in Fig. 11. The horizontal dimensions of the office room are shown in meters on the plan in Fig. 12, where the positions of the loudspeakers are represented by red circles and the position of the SFMA by a blue square. The height of the room is approximately 2.5 m and a mean reverberation time of 0.4 s was measured. The loudspeaker positions are chosen to mimic common sound event positions, such as opening a door, talking while sitting or standing. The loudspeaker position, with respect to the center of the array as the origin, is estimated using a laser telemeter. The ceiling of the room is composed of absorbent tiles where the one at the corner of interest is replaced by a wooden panel of the same dimensions on which the arrays are fixed. Moreover, one of the vertical walls forming the corner does not extend down to the floor. The effective size of the rigid boundaries is therefore limited.

#### 2. Beamforming result

The SRP calculation results for two loudspeaker positions are presented in Fig. 13 for each array. The first position is chosen to represent a sound event that takes place at the entrance of the room [Fig. 11(a)]. From this position, the acoustic sound impinges the array from the direction $(\phi_s, \theta_s) = (44.5°, 48.4°)$. The second position [Fig. 11(b)] is located on the top of the closest desk to the array, in the direction $(\phi_s, \theta_s) = (29.3°, 59.7°)$. This position is chosen

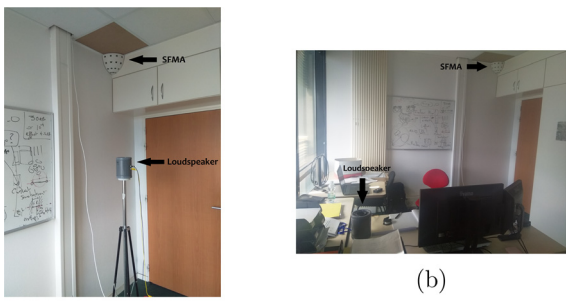


FIG. 11. (Color online) Loudspeaker positions placed in a conventional office room at the entrance (a) and on the closest desk from the array (b).

https://doi.org/10.1121/10.0009230

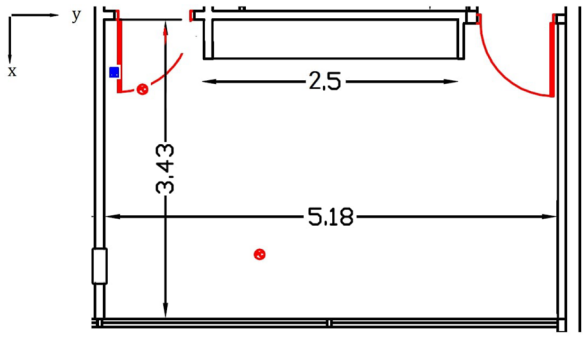


FIG. 12. (Color online) Plan of the conventional office room used for the measurements where the loudspeaker positions are indicated by red circles and the SFMA position by a blue square. The dimensions of the room are given in meters.

to simulate the sound events produced by a person working there. These positions are quite similar to positions (45°, 45°) and (60°, 60°), previously presented in the anechoic room case.

The results show similar performance criteria to those estimated experimentally in the anechoic room for the positions (45°, 45°) and (60°, 60°). It is worth noting that these results are satisfactory with regard to the measurement conditions. Indeed, on the one hand, the aforementionned rigidity boundary conditions of the one-eighth of space are not fully respected. On the other hand, the walls forming the corner are not perfectly perpendicular with gaps between the walls and the sides of the arrays on the order from 0.5 to 1 cm. Consequently, the sampling nodes of the one-eighth sphere and its images do not constitute the sampling of a perfect sphere and the actual SFH basis is not perfectly

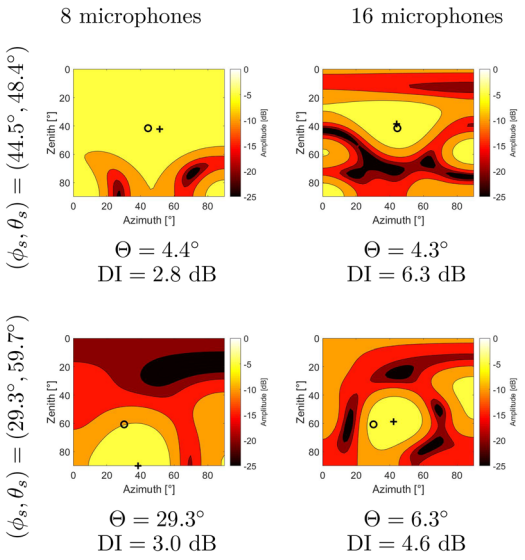


FIG. 13. (Color online) Comparison of the beamforming results with regular beampattern for two source DOAs from experimental measurements conducted in conventional office room. The normalized squared beamfomer output $|y(k,\theta,\phi)|^2/|y(k,\theta_s,\phi_s)|^2$ is plotted over the steering directions $(\theta,\phi) \in [0°, 90°] \times [0°, 90°]$ for $kr_a = 4.65$ for the 8-microphone array and $kr_a = 4.87$ for the 16-microphone array. The cross-and circle symbols represent the estimated and the theoretical source positions, respectively.

suitable. However, one observes good perfomance in the reported situation, which shows a certain robustness of the method despite the violation of some assumptions: acoustic rigidity and perfect geometry.

## V. CONCLUSION

This paper investigated the performance of one-eighth SFMAs to perform experimental acoustic scene analysis in a one-eighth of space based on SFH projection of the captured acoustic pressure. Two SFMAs with different radii and number of microphones were presented. The arrays were built using 3D printing where MEMS microphones were mounted on their shell. A study of spatial aliasing was investigated for both arrays through numerical simulations and analytical analysis. Measurements were conducted both in anechoic condition and in a conventional office room. Localization results showed accurate performances, close to the simulation ones, for both arrays, but with strong limitation to estimate source DOAs close to the walls. The results obtained in the conventional office room remain consistent with those obtained in the anechoic room, despite the presence of strong experimental constraints such as the limited zone in which the rigidity condition is respected.

## ACKNOWLEDGMENTS

This work was carried out in association with Orange Labs, France. The authors would like to thank Dr. Samuel Dupont for his help in theoretical background support. The authors would also like to thank the team of engineers composed of Pierre-Arnaud Lecomte, Stéphane Letourneur, Hervé Meziere, Jacky Maroudaye, and Eric Houliere who made the measurement bench.

## APPENDIX A: GAUSS-LEGENDRE QUADRATURE RULE IN $\mathbb{F}_{1/8}$

This appendix demonstrates that a Gauss-Legendre quadrature rule from Eq. (18) with odd degree $L$ is suitable in the one-eighth of a sphere $\mathbb{F}_{1/8}$ by retaining only the nodes belonging to $\mathbb{F}_{1/8}$.

Let us consider an acoustic pressure field $p(k,r,\theta,\phi)$ in the domain $\mathbb{O}_{1/8}$ with acoustical rigid condition of planes $x = 0$, $y = 0$, and $z = 0$. For simplicity, it is assumed that this pressure field does not have coefficients $p_{l,m,1/8}$ beyond degree $L$, that is to say,

$$p_{l,m,1/8} = 0 \quad \text{for} \quad l > L. \tag{A1}$$

This acoustic pressure field is sampled on the unit one-eighth of a sphere $\mathbb{F}_{1/8}$ at the nodes corresponding to a one-eighth of a Gauss-Legendre quadrature of odd degree $L$ belonging to $\mathbb{F}_{1/8}$. According to the image source principle,[21] an equivalent-free field problem can be considered: the planes $x = 0$, $y = 0$, and $z = 0$ are even symmetry planes for the acoustic pressure field and the nodes, as shown in Fig. 14. In the latter case, a whole Gauss-Legendre

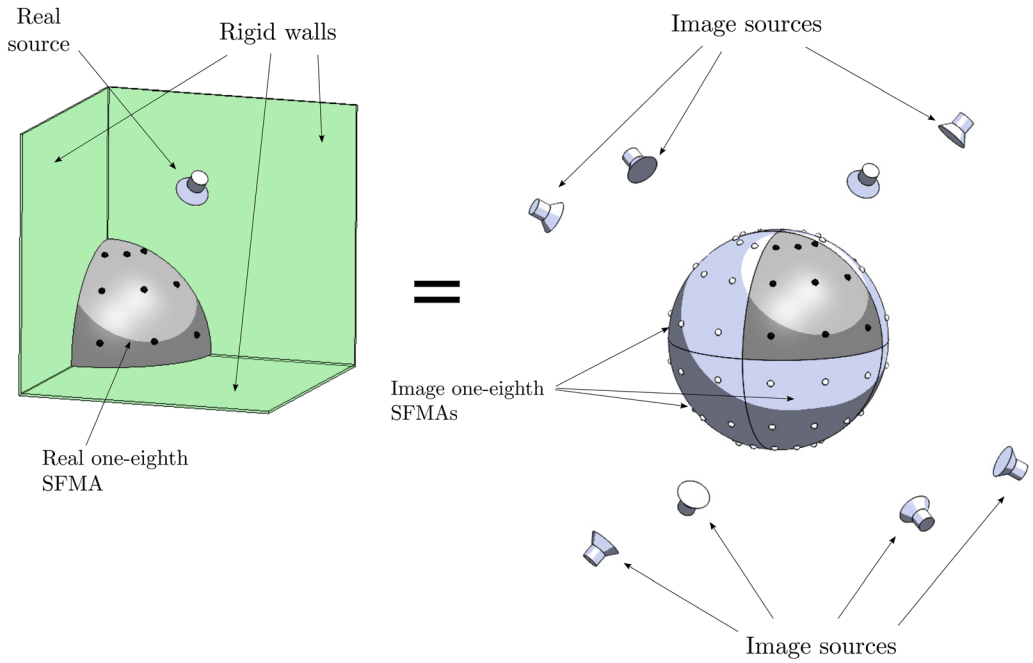


FIG. 14. (Color online) Image source principle for the $\mathbb{F}_{1/8}$ domain: a one-eighth SFMA (gray) with nine microphones (black nodes) is placed at a corner. The acoustic pressure field in the $\mathbb{F}_{1/8}$ domain is derived from the unbounded space where phenomena are symmetrized with respect to the rigid (green) planes $x = 0$, $y = 0$, and $z = 0$.

quadrature is obtained to sample a sound pressure field symmetric with respect to the planes $x = 0$, $y = 0$, and $z = 0$. For the Gauss-Legendre quadrature, the coefficients $p_{l,m}$ in $\mathbb{S}$ are given by

$$\begin{aligned} p_{l,m} &= \sum_{n=0}^{2L+1}\sum_{q=0}^{L}\alpha_q p(k,r,\theta_q,\phi_n)Y_{l,m}(\theta_q,\phi_n) \\ &= \int_{\mathbb{S}} p(k,r,\theta,\phi)Y_{l,m}(\theta,\phi)\sin(\theta)\mathrm{d}\theta\mathrm{d}\phi. \end{aligned} \tag{A2}$$

According to Eq. (18), the zenith angles $\theta_q$ correspond to the roots of the Legendre polynomial $P_{L+1}(\cos(\theta))$. The function $P_{L+1}$ being even, the corresponding zenith angles $\theta_q$ are symmetrically distributed around the angle $\theta = \pi/2$, which corresponds to the plane $z = 0$. The sum in Eq. (A2) is then rewritten as follows:

$$\begin{aligned} p_{l,m} = &\sum_{n=0}^{2L+1}\sum_{q=0}^{(L-1)/2}\alpha_q p(k,r,\theta_q,\phi_n)Y_{l,m}(\theta_q,\phi_n) \\ &+\alpha_{q'}p(k,r,\theta_{q'},\phi_n)Y_{l,m}(\theta_{q'},\phi_n), \end{aligned} \tag{A3}$$

with

$$\begin{aligned} q' &= q + (L+1)/2 \\ \theta_{q'} &= \pi - \theta_q \\ \alpha_{q'} &= \alpha_q \\ p(k,r,\theta_{q'},\phi_n) &= p(k,r,\theta_q,\phi_n) \\ Y_{l,m}(\theta_{q'},\phi_n) &= (-1)^{l+m}Y_{l,m}(\theta_q,\phi_n). \end{aligned} \tag{A4}$$

Thus, Eq. (A3) can be simplified to

$$p_{l,m} = (1+(-1)^{l+m})\sum_{n=0}^{2L+1}\sum_{q=0}^{(L-1)/2}\alpha_q p(k,r,\theta_q,\phi_n)Y_{l,m}(\theta_q,\phi_n), \tag{A5}$$

where Eq. (A5) shows that if $l+m$ is odd, $p_{l,m} = 0$ and if $l+m$ is even, the quadrature rule result is twice the result of the quadrature rule applied on a half of sphere, i.e., only the zenith angle $\theta_q$ for $q \in \{0 \cdots (L-1)/2\}$. Following the same reasoning by exploiting the symmetry properties of SHs[16] and of the acoustic pressure field with respect to plane $x = 0$ and $y = 0$, it is shown that

$$p_{l,m} = \begin{cases} 8\displaystyle\sum_{n=0}^{(L-1)/2}\sum_{q=0}^{(L-1)/2}\alpha_q p(k,r,\theta_q,\phi_n)Y_{l,m}(\theta_q,\phi_n) \\ \quad \text{for } (l,m) \in \mathbb{M}_{1/8} \\ 0 \quad \text{for } (l,m) \notin \mathbb{M}_{1/8}. \end{cases} \tag{A6}$$

In the same manner as Appendix E of Ref. 16, one can show as well that

$$p_{l,m} = \begin{cases} 8\displaystyle\int_{\mathbb{F}_{1/8}} p(k,r,\theta,\phi)Y_{l,m}(\theta,\phi)\sin(\theta)\mathrm{d}\theta\mathrm{d}\phi \\ \quad \text{for} \quad (l,m) \in \mathbb{M}_{1/8} \\ 0 \quad \text{for} \quad (l,m) \notin \mathbb{M}_{1/8}. \end{cases} \tag{A7}$$

Using Eq. (3) in Eq. (A7) and identifying with Eq. (9), one obtains

$$p_{l,m} = \begin{cases} 2\sqrt{2}p_{l,m,1/8} & \text{for} \quad (l,m) \in \mathbb{M}_{1/8} \\ 0 & \text{for} \quad (l,m) \notin \mathbb{M}_{1/8}. \end{cases} \tag{A8}$$

Finally, using Eq. (3) in Eq. (A6) and identifying with Eq. (A8), it is shown that

https://doi.org/10.1121/10.0009230

$$p_{l,m,1/8} = \sum_{n=0}^{(L-1)/2} \sum_{q=0}^{(L-1)/2} \alpha_q p(k,r,\theta_q,\phi_n) Y_{l,m,1/8}(\theta_q,\phi_n). \quad \text{(A9)}$$

Equation (A9) shows that using the Gauss-Legendre quadrature rule of degree $L$ odd, retaining only the nodes belonging to $\mathbb{F}_{1/8}$ and using SFHs $Y_{l,m,1/8}$, it is possible to obtain the coefficients $p_{l,m,1/8}$.

## APPENDIX B: ALIASING FUNCTION DEMONSTRATION

In this appendix, the conditions on the indices $(l, l', m, m')$ for the aliasing function $\epsilon(l, l', m, m')$ to be null in Eq. (22) are demonstrated. The equation Eq. (22) is rewritten using the real SHs constrained to the indices $(l, m) \in \mathbb{M}_{1/8}$ by replacing the SFHs expression given in Eq. (3)

$$\begin{aligned} &8 \sum_{n=0}^{(L-1)/2} \sum_{q=0}^{(L-1)/2} \alpha_q Y_{l,m}(\theta_q,\phi_n) Y_{l',m'}(\theta_q,\phi_n) \\ &\quad = \delta_{l-l'}\delta_{m-m'} + \epsilon(l,l',m,m'). \end{aligned} \quad \text{(B1)}$$

Replacing the expression of the real SHs[16] in the latter equation leads to

$$\begin{aligned} &8 N_{l,|m|} N_{l',|m'|} \sum_{n=0}^{(L-1)/2} \cos(m\phi_n) \cos(m'\phi_n) \\ &\quad \times \sum_{q=0}^{(L-1)/2} \alpha_q P_l^m(\cos(\theta_q)) P_{l'}^{m'}(\cos(\theta_q)) \\ &\quad = \delta_{l-l'}\delta_{m-m'} + \epsilon(l,l',m,m'), \end{aligned} \quad \text{(B2)}$$

where $P_l^m$ are the associated Legendre polynomial of the first kind of degree $l$ and order $m$ and $N_{l,|m|} = \sqrt{(2-\delta_m)(2l+1)(l-|m|)!/(4\pi(l+|m|)!)}$, is a normalization factor ensuring the orthonormality of the SHs on the unit sphere. Note that Eq. (B2) is obtained for $m \geq 0$ as constrained by $\mathbb{M}_{1/8}$. From Eq. (B2), it can be seen that the aliasing function is null if the Kronecker product is null, i.e., if $l \neq l'$ or $m \neq m'$, and if the left product is also null, i.e., if at least one of the sums is null,

$$\sum_{n=0}^{(L-1)/2} \cos(m\phi_n) \cos(m'\phi_n) = 0, \quad \text{(B3)}$$

or

$$\sum_{q=0}^{(L-1)/2} \alpha_q P_l^m(\cos(\theta_q)) P_{l'}^{m'}(\cos(\theta_q)) = 0. \quad \text{(B4)}$$

### 1. Solutions of Eq. (B3)

By replacing the expression of the azimuth angle given in Eq. (18) and using trigonometric formulas, Eq. (B3) can be rewritten as follows:

$$\begin{aligned} &\frac{1}{2} \sum_{n=0}^{(L-1)/2} \cos\left((m+m')\left(n+\frac{1}{2}\right)\frac{\pi}{L+1}\right) \\ &+\frac{1}{2} \sum_{n=0}^{(L-1)/2} \cos\left((m-m')\left(n+\frac{1}{2}\right)\frac{\pi}{L+1}\right) = 0. \end{aligned} \quad \text{(B5)}$$

The latter equation involves the sum of cosines with arguments in arithmetic progression[22] that can be reduced to

$$\begin{aligned} &\frac{\sin\left((m+m')\frac{\pi}{2}\right)}{\sin\left((m+m')\frac{\pi}{2L+2}\right)} + \frac{\sin\left((m-m')\frac{\pi}{2}\right)}{\sin\left((m-m')\frac{\pi}{2L+2}\right)} = 0 \\ &\text{for } \frac{(m+m')\pi}{2L+2} \neq k\pi \wedge \frac{(m-m')\pi}{2L+2} \neq k\pi \wedge k \in \mathbb{Z}. \end{aligned} \quad \text{(B6)}$$

In order to solve Eq. (B6), let $f_L[n]$, $n \in 2\mathbb{Z}$, be the following discrete function:

$$f_L[n] = \frac{\sin\left(\frac{n\pi}{2}\right)}{\sin\left(\frac{n\pi}{2L+2}\right)}. \quad \text{(B7)}$$

The equation Eq. (B6) is therefore reduced to

$$f_L[m+m'] + f_L[m-m'] = 0. \quad \text{(B8)}$$

From the L'Hôpital's rule, it can be shown that

$$\begin{cases} \lim\limits_{n \to 0 \bmod 4L+4} f_L[n] = L+1 \\ \lim\limits_{n \to 2L+2 \bmod 4L+4} f_L[n] = -L-1. \end{cases} \quad \text{(B9)}$$

As well, it can be shown that the function $f_L[n]$ is periodic of period $4L+4$ and that $f_L[n] = 0$ for $n \bmod (2L+2) \neq 0$. The discrete function $f[n]$ is therefore explicitly given by

$$f_L[n] = \begin{cases} L+1 & \text{for} \quad n \bmod (4L+4) = 0 \\ -L-1 & \text{for} \quad n+2L+2 \bmod (4L+4) = 0 \\ 0 & \text{for} \quad n \bmod (2L+2) \neq 0. \end{cases} \quad \text{(B10)}$$

Finally, from Eq. (B10), the solutions of Eq. (B8), i.e., Eq. (B3), are

$$\begin{aligned} &f_L[m+m'] + f_L[m-m'] \\ &= \begin{cases} 0 & \text{for } (m+m') \bmod (4L+4) = 0 \\ & \quad \wedge (m-m'+2L+2) \bmod (4L+4) = 0 \\ 0 & \text{for } (m+m'+2L+2) \bmod (4L+4) = 0 \\ & \quad \wedge (m-m') \bmod (4L+4) = 0 \\ 0 & \text{for } (m+m') \bmod (2L+2) \neq 0 \\ & \quad \wedge (m-m') \bmod (2L+2) \neq 0. \end{cases} \end{aligned} \quad \text{(B11)}$$

### 2. Solutions of Eq. (B4)

In Appendix A, it was shown for odd degree $L$, that the Gauss-Legendre quadrature for the one-eighth of a sphere

with rigid boundary conditions is equivalent to the Gauss-Legendre quadrature on the whole sphere for a symmetric function to integrate. However, Eq. (B4) adapted for the whole sphere is solved in Ref. 20 when $l+l'$ is odd. In the present case, $l+l'$ is never odd as $(l,l') \in \mathbb{M}^2_{1/8}$, which ensures the symmetry of $Y_{l,m,1/8}$ function. Therefore, Eq. (B4) has no solutions for $(l,m,l',m') \in \mathbb{M}^4_{1/8}$.

### 3. Aliasing function nullity conditions

The Gauss-Legendre quadrature of Eq. (18) guarantees no aliasing when $l+l' \leq 2L+1$.[20] Finally, for a quadrature working for $l \leq L$ the aliasing function satisfies

$$\epsilon(l,l',m,m') = \begin{cases} 0 \ \text{for} \ l+l' \leq 2L+1 \\ 0 \ \text{for} \ (m+m') \bmod (4L+4) = 0 \\ \quad \wedge (m-m'+2L+2) \bmod (4L+4) = 0 \\ 0 \ \text{for} \ (m+m'+2L+2) \bmod (4L+4) = 0 \\ \quad \wedge (m-m') \bmod (4L+4) = 0 \\ 0 \ \text{for} \ (m+m') \bmod (2L+2) \neq 0 \\ \quad \wedge (m-m') \bmod (2L+2) \neq 0. \end{cases} \quad \text{(B12)}$$


[1] J. Benesty, J. Chen, and Y. Huang, *Microphone Array Signal Processing*, Vol. 1 (Springer Science & Business Media, New York, 2008).
[2] P. Lecomte, P.-A. Gauthier, C. Langrenne, A. Berry, and A. Garcia, "Cancellation of room reflections over an extended area using ambisonics," J. Acoust. Soc. Am. **143**(2), 811–828 (2018).
[3] J. Lopez-Marulanda, O. Adam, T. Blanchard, M. Vallée, D. Cazau, and F. Delfour, "First results of an underwater 360° HD audio-video device for etho-acoustical studies on bottlenose dolphins (tursiops truncatus)," Aquatic Mamm. **43**(2), 162–176 (2017).
[4] T. Blanchard, J.-H. Thomas, and K. Raoof, "Acoustic localization and tracking of a multi-rotor unmanned aerial vehicle using an array with few microphones," J. Acoust. Soc. Am. **148**(3), 1456–1467 (2020).
[5] S. Moreau, J. Daniel, and S. Bertet, "3D sound field recording with higher order ambisonics–Objective measurements and validation of a 4th order spherical microphone," in *Proceedings of the 120th AES Convention*, Paris, France (May 20–23, 2006), pp. 20–23.
[6] B. Rafaely, "Acoustical background," in *Fundamentals of Spherical Array Processing* (Springer, New York, 2019), pp. 33–58.
[7] J. Meyer and G. Elko, "A highly scalable spherical microphone array based on an orthonormal decomposition of the soundfield," in *Proceedings of the 2002 IEEE International Conference on Acoustics, Speech, and Signal Processing*, Orlando, FL (May 13–17, 2002), pp. 1781–1784.
[8] Z. Li and R. Duraiswami, "Hemispherical microphone arrays for sound capture and beamforming," in *IEEE Workshop on Applications of Signal Processing to Audio and Acoustics 2005*, New Paltz, New York (October 16–19, 2005). pp. 106–109.
[9] F. Zotter and H. Pomberger, "Spherical slepian functions for approximation of spherical measurement data," in *Fortschritte Der Akustik - DAGA*, Darmstadt, Germany (March 19–22, 2012).
[10] P. Gautron, J. Krivánek, S. N. Pattanaik, and K. Bouatouch, "A novel hemispherical basis for accurate and efficient rendering," Rendering Tech. **2004**, 321–330 (2004).
[11] D. Kumari and L. Kumar, "Spherical sector harmonics representation of sound fields using a microphone array over spherical sector," J. Acoust. Soc. Am. **149**(1), 145–157 (2021).
[12] H. Pomberger, "Acoustic boundary value problems and their application to partial spherical microphone arrays," Ph.D. thesis, University of Music and Performing Arts Graz, Graz, Austria (2017).
[13] H. Pomberger and F. Zotter, "Modal sound field decomposition applicable for a limited range of directions," in *Fortschritte Der Akustik, AIA-DAGA*, Merano, Germany (March 18–21, 2013).
[14] H. Pomberger and F. Pausch, "Design and evaluation of a spherical segment array with double cone," Acta Acust. united Ac. **100**(5), 921–927 (2014).
[15] B.-D. Keller and F. Zotter, "A new prototype for sound projection," in *Forstschritte Der Akustik - DAGA*, Nürnberg, Germany (March 16–19, 2015).
[16] P. Lecomte, M. Melon, and L. Simon, "Spherical fraction beamforming," IEEE/ACM Trans. Audio Speech Lang. Process. **28**, 2996–3009 (2020).
[17] P. Lecomte, T. Blanchard, M. Melon, L. Simon, K. Hassan, and R. Nicol, "One-eighth of a sphere microphone array," in *Proceedings of the e-Forum Acusticum*, Online (December 7–11, 2020).
[18] B. Rafaely, "Analysis and design of spherical microphone arrays," IEEE Trans. Speech Audio Process. **13**(1), 135–143 (2005).
[19] P. Lecomte, P.-A. Gauthier, C. Langrenne, A. Berry, and A. Garcia, "A fifty-node Lebedev grid and its applications to ambisonics," J. Audio Eng. Soc. **64**(11), 868–881 (2016).
[20] B. Rafaely, B. Weiss, and E. Bachmat, "Spatial aliasing in spherical microphone arrays," IEEE Trans. Signal Process. **55**(3), 1003–1010 (2007).
[21] P. M. Morse and K. U. Ingard, *Theoretical Acoustics* (Princeton University Press, Princeton, NJ, 1986).
[22] M. P. Knapp, "Sines and cosines of angles in arithmetic progression," Math. Mag. **82**, 371–372 (2009).